The Astrophysical Journal Letters, 984:L24 (5pp), 2025 May 1 https://doi.org/10.3847/2041-8213/adc9aa

A Model-independent Radio Telescope Dark Matter Search in the *L* and *S* Bands

Aya Keller[1], Nicole Wolff[2], and Karl van Bibber[1]
[1] Department of Nuclear Engineering, University of California, Berkeley, CA 94709, USA; ayakeller@berkeley.edu
[2] Department of Physics, Columbia University, NY 10027, USA
Received 2025 March 4; revised 2025 April 3; accepted 2025 April 4; published 2025 April 30

Abstract

Ultralight bosonic dark matter in its most general form can be detected through its decay or annihilation to a quasimonochromatic radio line. Assuming only that this line is consistent with the most general properties of the expected phase space of our Milky Way halo, we have developed and carried out a novel model-independent search for dark matter in the *L* and *S* bands. More specifically, the search selects for a line that exhibits a Doppler shift with position according to the solar motion through a static halo and similarly varies in intensity with position with respect to the Galactic center. Over the combined *L*- and *S*-band range 1020–2700 MHz, radiative annihilation of dark matter is excluded above $\langle \sigma v \rangle \approx 10^{-30}\,\mathrm{cm^3\,s^{-1}}$, and for decay above $\lambda \approx 10^{-32}\,\mathrm{s^{-1}}$.

Unified Astronomy Thesaurus concepts: Dark matter (353); Technosignatures (2128); Radio astronomy (1338); Doppler shift (401)

1. Introduction

While the overwhelming evidence for the existence of dark matter continues to build, progress toward its identification remains limited. In recent years, advances in detector technology have enabled a new generation of experiments that are exquisitely sensitive to specific well-motivated dark matter candidates; see E. Aprile et al. (2019) for weakly interacting massive particle dark matter and K. M. Backes et al. (2021) in the realm of axionic dark matter. While these latter experiments based on the resonant conversion of ultralight dark matter have been able to successfully exclude regions within a decade of mass, theoretical bounds have recently been relaxed by several orders of magnitude, giving rise to an even more broad range of possible axion masses. Furthermore, attention has recently been shifting to a theoretical framework for dark matter that does not assume specific models. An optimal analysis strategy should thus rely on as few general assumptions as possible, while possessing a high degree of selectivity and sensitivity to dark matter.

This search focuses on the possible radiative decay or annihilation of ultralight dark matter within our Milky Way Galactic halo, leading to a quasimonochromatic radio line ($\Delta\nu/\nu \approx 10^{-3}$). This search is further predicated on two generally accepted characteristics of dark matter in our Galactic halo. First, we assume that the dark matter constitutes a static halo through which our solar system is moving, with a characteristic velocity $v_S \approx 240\,\mathrm{km\,s^{-1}}$ tangential to the disk. Consequently, such a radio line would be distinguished from any other source, conventional or otherwise, by a systematic Doppler shift with respect to the Sun's direction of motion: $(l,\ b) = (90^\circ,\ 0^\circ)$ in Galactic coordinates. Second, the signal should reflect the spatial distribution as represented by a standard halo model. More specifically the signal power should follow the line-integrated density of the halo ρ for dark matter decay or ρ^2 for annihilation or any other two-body process producing a photon, maximized toward the Galactic center, $(0^\circ,\ 0^\circ)$, minimized looking outward, and roughly symmetric around that axis.

Dark matter decay here includes all processes $\chi \rightarrow \phi + \gamma$, including in principle two-photon decays from pseudoscalars such as the axion or an axion-like particle $\chi \rightarrow \gamma + \gamma$. What we refer to as annihilation includes all two-body initial states, including annihilation proper $\chi + \chi \rightarrow \phi + \gamma$ as well as Compton-like processes $\chi + \xi \rightarrow \phi + \gamma$, where ξ and ϕ represent any standard model or beyond-standard model particles.

We report here an analysis based on this strategy in the *L* and *S* band, utilizing the Breakthrough Listen (BL) public data release from the 100 m Robert C. Byrd Green Bank Telescope (GBT), which was taken between 2016 January and 2019 March (M. Lebofsky et al. 2019; D. C. Price et al. 2020). The analysis concept and proof of principle appeared in an earlier publication over a very narrow frequency range in the *L* band (A. Keller et al. 2022), but as several improvements and optimizations have been made subsequently, the current analysis will be described below.

2. Analysis

The analysis includes 5433 spectra in the *S* band and 4400 in the *L* band. The primary spectra of 2.8610 kHz channel resolution display an undulatory structure of order 10 MHz imprinted with the polyphase filterband function (PPF), a symmetric periodic function defining coarse channels of 2.9307 MHz. The spectra are first coaveraged from the original 1024 channels by 64. After dividing out the PPF, the spectra need to be unit normalized. An ideal normalization scheme would be able to simultaneously track a putitive signal atop the raw data and interpolate the background structure assuming no signal is there. After an investigation of different normalization techniques and functional forms, the best scheme was determined to be a ratio-of-function fit within a window around each data point in the spectrum:

$$R(\nu_i) = \frac{G(\nu_i;\,\sigma) + P(\nu_i;\,m,\,n)}{P_D(\nu_i;\,m,\,n)}. \tag{1}$$

For the polynomial $P(\nu_i;\,m,\,n)$ fit to the data within a window around ν_i, m is the number of data points within the window, and n is the order of the polynomial. The values $(m,\,n) = (55,$

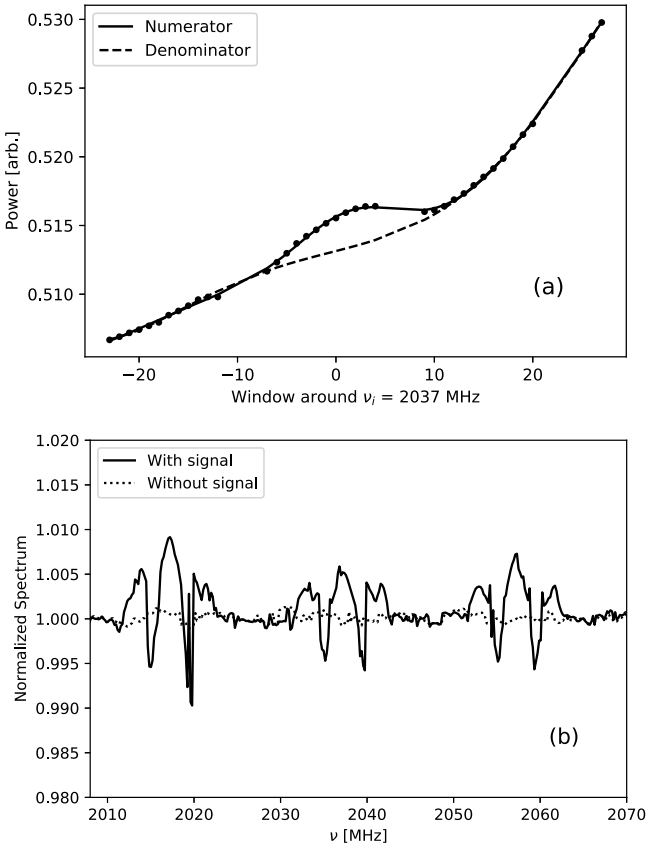

Figure 1. (a) A synthetic signal from dark matter decay with decay constant $\lambda = 1 \times 10^{-30}\ \mathrm{s}^{-1}$ injected into one raw spectrogram, with the numerator and denominator components of the normalization function plotted at a single-point snapshot of the moving normalization. (b) A normalized spectrum with three injected signals spaced 20 MHz apart.

5) were selected on the basis of maximizing the signal to noise of the spectral asymmetry for synthetic signals injected into the spectrum, as described below. For the Gaussian function $G(\nu_i; \sigma)$, σ is specified based on the expected width of the signal at ν_i, and the coefficient and center frequency are left as free parameters for the fit (with the condition that the coefficient is positive). The polynomial in the denominator, $P_D(\nu_i; m, n)$, is the same functional form as that in the numerator, but where a window representing the expected signal width around the center of the Gaussian is blanked out for the fit.

$$G(\nu_i; \sigma) = a^2 \cdot \exp\left[\frac{-(\nu - \nu_i)^2}{2\sigma^2}\right], \tag{2}$$

$$P(\nu_i; m, 5) = b + c \cdot \nu_i + d \cdot \nu_i^2 + f \cdot \nu_i^3 + g \cdot \nu_i^4 + h \cdot \nu_i^5. \tag{3}$$

When the moving window is centered on a real signal, this procedure ensures that the sum of the polynomial and Gaussian in the numerator more closely tracks the signal atop the local background, whereas the polynomial in the denominator excludes the signal, thus more faithfully interpolating the real background in the absence of such a signal, as portrayed in Figure 1(a). However, as can be readily seen, when the center of the moving window is offset from a real signal, the interpolated background can lie above the actual data, resulting in an undershoot in the normalized data. A Gaussian signal will thus be transformed into a more complex form, as seen in Figure 1(b). This does not represent any difficulty in the analysis, as the transform is deterministic and the ultimate physics limits are set by following injected signals all the way through the analysis chain.

The concept of the Doppler and Intensity asymmetries is schematically represented in Figure 2. In the case of the Doppler asymmetry, under the assumption of a static halo, a dark matter signal is Doppler shifted according to its polar angle θ from the direction of the Sun's motion through the Galaxy:

$$\nu' = \nu\left(1 + \frac{V_S}{c} \cdot \cos\theta\right), \tag{4}$$

where estimates for the solar velocity $V_S \approx 240\ \mathrm{km\ s^{-1}}$ (G. Monari et al. 2018) are comparable to the local virial velocity of the galaxy, $\sigma_{\mathrm{vir}} \approx 270\ \mathrm{km\ s^{-1}}$ (A. Pillepich et al. 2014). Owing to the observational and modeling uncertainties intrinsic to these numbers, we explored the variation of our analysis with excursions of V_S and σ_{vir} within the range 225–275 $\mathrm{km\ s^{-1}}$ and find it to be not highly sensitive.

For each case, the asymmetry spectrum is formed:

$$A_D(\nu) = \frac{F - B}{F + B} \quad A_I(\nu) = \frac{I - O}{I + O}, \tag{5}$$

with F (B) designating the average of all spectra within the Forward (Backward) acceptances defined by their polar angles $\theta_{F/B}$.

$$F(\nu, \theta_F) = \frac{1}{n_f}\sum_i f_i(\nu) \quad B(\nu, \theta_B) = \frac{1}{n_b}\sum_i b_i(\nu) \tag{6}$$

for some fixed θ_F and θ_B and similarly for I (O), the Inward (Outward) populations within their respective polar angle cuts $\Phi_{I/O}$. Forming asymmetry spectra has the virtue of canceling out to a high degree the common-mode residual structure apparent in all normalized spectra at the $\approx 10^{-4}$ level, thus enabling a more sensitive search.

See E. G. Speckhard et al. (2016) for the suggested utility of Doppler shift in determining the source of the 3.5 keV line reported by several X-ray observatories at the time.

The flux density in general for the two cases of annihilation and decay processes is given by

$$\frac{P_A}{\Delta A \Delta\nu} = \frac{1}{8\sqrt{2\pi}} \frac{\langle\sigma v\rangle (\Delta\theta)^2 c^2}{M_\chi \eta^A \nu_0} e^{\left[-\left(\frac{\nu-\nu_0}{\sqrt{2}\eta^A\nu_0}\right)^2\right]} \int_0^\infty \rho(\boldsymbol{r})^2\, d\boldsymbol{r}, \tag{7}$$

$$\frac{P_D}{\Delta A \Delta\nu} = \frac{1}{16\sqrt{2\pi}} \frac{\lambda (\Delta\theta)^2 c^2}{\eta^D \nu_0} e^{\left[-\left(\frac{\nu-\nu_0}{\sqrt{2}\eta^D\nu_0}\right)^2\right]} \int_0^\infty \rho(\boldsymbol{r})\, d\boldsymbol{r}, \tag{8}$$

which depends on the particle physics through the velocity-weighted cross section $\langle\sigma v\rangle$ for annihilation or the decay constant λ in the case of decay. Here $\rho(\boldsymbol{r})$ is the halo density along the line of sight, $\Delta\theta$ the frequency-dependent FWHM beamwidth of the telescope, and η the line width, with σ_{vir} the

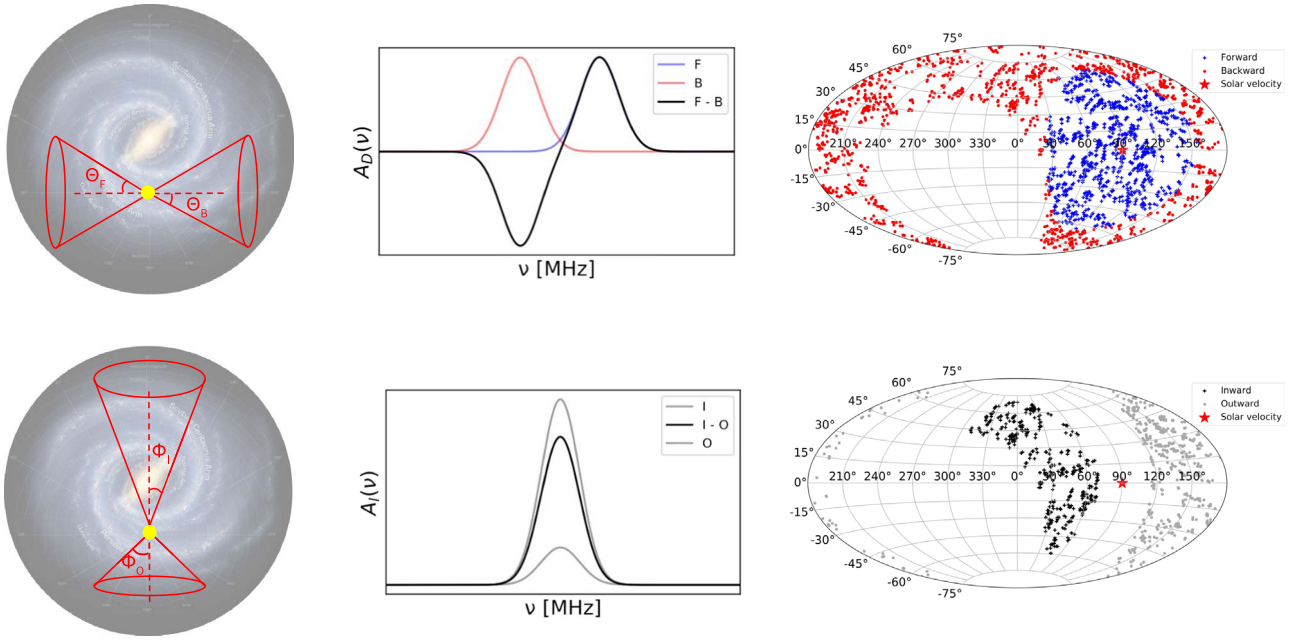

Figure 2. (a) Concept of asymmetry-based searches for dark matter within a large data set broadly sampling the observable sky. The angles defining the Forward and Backward samples, $\theta_{F,B}$ are chosen to maximize the S/N. (b) The idealized dark matter signature in the Doppler asymmetry spectrum $A_D(\nu)$ would be a bipolar signal in frequency, prescribed by the (V_S, $\sigma_{\rm vir}$) and the ensemble of specific targets selected. The idealized dark matter signature in the Intensity asymmetry spectrum $A_I(\nu)$ would be a unipolar signal centered at the frequency of the decay or annihilation photon in the dark matter's rest frame. In practice, due to the normalization scheme, the actual asymmetries are more complex in shape but remain antisymmetric and symmetric, respectively. (c) Mercator plots exhibiting the actual targets included in the analysis, the regions being demarked by $\theta_F = \theta_B = 65^\circ$ and $\Phi_I = 70^\circ$, $\Phi_O = 115^\circ$ (adapted from A. Keller et al. 2022).

halo virial velocity,

$$\eta^A = \frac{\sigma_{\rm vir}}{\sqrt{6}\,c},\ \eta^D = \frac{\sigma_{\rm vir}}{\sqrt{3}\,c}. \tag{9}$$

For simplicity, these formulae are written for the special case of a two-photon final state, i.e., $\chi\chi \rightarrow \gamma\gamma$ and $\chi \rightarrow \gamma\gamma$, for which the resulting limits will be seen to be much weaker than allowed by stellar evolution but are readily convertible to limits for final states with a massive particle $\phi\gamma$.

The resulting limits are derived by a standard matched-filtering technique. A template of the asymmetry for a dark matter signal is created at each frequency ν in the spectrum, $\boldsymbol{T}(\nu)$, specific to the particle physics input $\langle\sigma v\rangle$ or λ, target samples $\theta_{F/B}$, Galactic parameters (V_S, $\sigma_{\rm vir}$), and halo model. At each frequency ν the template is integrated over the asymmetry spectrum:

$$R_D(\nu) = \boldsymbol{T}\cdot\boldsymbol{A_D}(\boldsymbol{\nu}) \equiv \sum_{\nu'} T(\nu-\nu')A_D(\nu-\nu'), \tag{10}$$

resulting in the Doppler correlation spectrum $R_D(\nu)$.

Limits are derived by injecting synthetic signals at the raw spectrogram level, carrying through the analysis as described, and establishing the confidence level against the statistical distribution of $R(\nu)$ in the absence of a signal. The signal-to-noise ratio (S/N) is maximized by utilizing all of the data after the data quality cut and equalizing the Forward and Backward populations, corresponding to the polar angle $\theta_F = \theta_B = 65^\circ$.

In a completely analogous way, the Intensity analysis is based on the expected signal asymmetry between looking inward (I), toward the Galactic center, and outward (O), away from the Galactic center. Here, the S/N is maximized by more tightly restricting the cone defining the inward population and leaving a large gap in angle ($\Phi_I = 70^\circ \Phi_O = 115^\circ$). For this analysis, a Navarro–Frenk–White (NFW) halo was used (J. F. Navarro et al. 1997; F. Nesti & P. Salucci 2013):

$$\rho(r) = \rho_c \left(\frac{r}{r_c}\right)^{-1}\left(1+\frac{r}{r_c}\right)^{-2}, \tag{11}$$

with $\rho_c = 1.4 \times 10^7\, M_\odot\,{\rm kpc}^{-3}$ and $r_c = 16.1$ kpc.

Stronger limits can be achieved by cross-correlating the Doppler and Intensity analyses, first making sure that the two analyses are absolutely independent. In particular, it is most important to ensure that there are no remnant velocity correlations inadvertently built into the I,O populations of the Intensity analysis, owing to the incomplete GBT Galactic coverage (Figure 2). To ensure that the total I,O contributions (Equation (6)) were coincident in frequency, that is, free of residual Doppler shift, while maximizing the number of spectra selected, the Hungarian matching algorithm is used for annihilation, and a manual shift of the signal is used for decay as the decay signal is too wide to necessitate the matching (H. W. Kuhn 1955).

3. Results

How dark matter decay would appear in the data is represented in Figure 3, where a synthetic signal has been injected into each S-band spectrum for the case of $V_S = 225\ {\rm km\,s^{-1}}$, $\sigma = 250\ {\rm km\,s^{-1}}$, $\lambda = 1 \times 10^{-30}\ {\rm s^{-1}}$, and the intensity corresponding to the NFW halo described above at Galactic coordinates (l, b). The results of the separate Doppler and Intensity analyses can be combined to yield stronger limits on halo dark matter. As the analyses are independent and their individual template correlation spectra are approximately Gaussian distributed, application of the p-test on the cross correlation of the two analyses is straightforward (Figure 4).

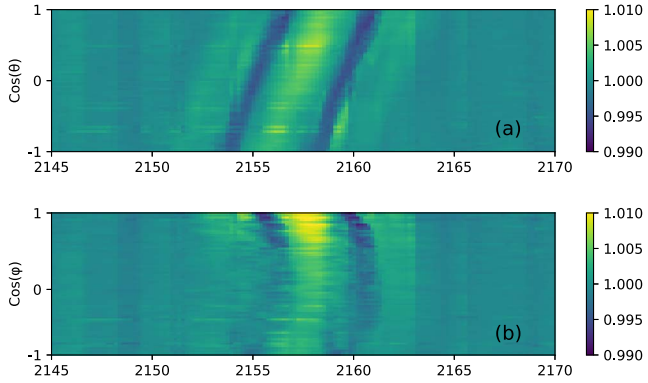

Figure 3. False-color maps of normalized spectra sorted by features of the data corresponding to the Doppler and Intensity analyses: (a) θ (angle from the Sun's direction of motion), Φ (angle from the Galactic center) for a signal of size $\lambda = 1 \times 10^{-30}\,\mathrm{s}^{-1}$.

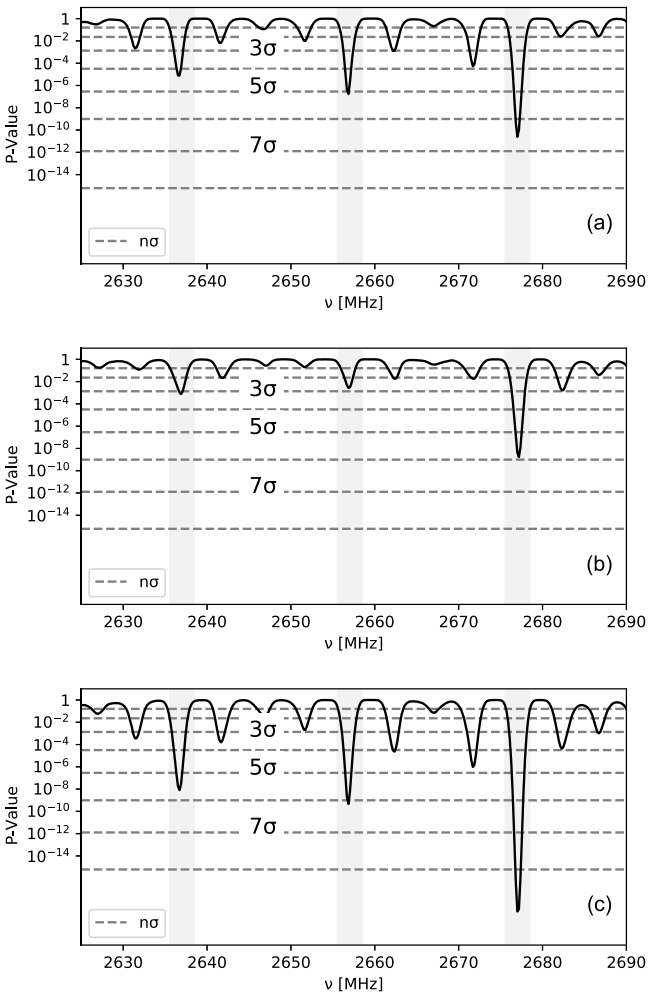

Figure 4. The p-statistic for three injected signals over a clean region in the S band for the decay case; $\lambda = 1 \times 10^{-30}\,\mathrm{s}^{-1}$. (a) Doppler p-value spectrum, (b) Intensity p-value spectrum, (c) combined p-value spectrum.

Three comments are in order concerning determination of the limits. First, as the BL data set was lacking in any useful calibration targets, the system equivalent flux density was calculated from the published GBT L- and S-band system noise temperature of $T_{\mathrm{SYS}} = 20\,\mathrm{K}$ and aperture efficiency 70%. To check our absolute calibration, a comparison was made of the inferred H I column density measured in our data with data from the Bonn Library (B. Ben et al. 2016). The inferred value is within 1.5% of the older Leiden/Argentine/Bonn survey and 15% higher than the newer Effelsburg/Bonn H I survey, thus giving us confidence in our procedure. Second, the limit above was derived with a search template of the same Galactic halo parameters as the injected signal, $(V_S,\ \sigma_{\mathrm{vir}}) = (225,\ 250)$ [km s^{-1}]. As we have no precise a priori knowledge of the halo parameters, we tested two additional cases in the L band within current bounds of solar and virial velocities, $(V_S,\ \sigma_{\mathrm{vir}}) = (225,\ 250),\ (200,\ 250),\ (225,\ 275)$ [km s^{-1}]. By mismatching the injection and search parameters, we measured the sensitivity of our search to our ignorance of these parameters, the resulting limits differing by about 10% on average. Third, it may be inquired to what degree the physics exclusion limits depend on the exact choice of halo model. We have performed such a comparison between those derived from the NFW halo described above and those from a Burkert halo, parameters of which were determined by fitting to the same Milky Way Galactic observables by the same authors (F. Nesti & P. Salucci 2013). While both yield essentially the same local density, the quantity of interest to direct detection experiments, $\rho^{\mathrm{NFW}}(r_s) = 0.471$ and $\rho^{\mathrm{Bur}}(r_s) = 0.487\,\mathrm{GeV\,cm^{-3}}$, their virial masses M_{vir} differ considerably, 1.53×10^{12} and $1.11 \times 10^{12}\,M_s$, respectively. Correspondingly, the limit on the annihilation cross section at 1775 MHz for the Burkert model is 60% weaker than that for NFW halo, the annihilation rate going as ρ^2.

Resulting limits of annihilation and decay are shown in Figure 5. These were calculated by reducing the injected signal until the resulting combined p-value reached 3σ for each frequency window of 5 MHz. Any other candidates above 3σ were excluded by investigation of RFI, temporal correlations, and lack of a systematic Doppler shift.

These limits also include the effect of stimulated emission. A. Caputo et al. (2019) have calculated the stimulated emission of axions within the radiation background of our Galactic halo, but the results are readily generalized to any process with a photon in the final state. Specifically, the enhancement for the rate or cross section is a simple multiplicative factor of $2f_\gamma$ or f_γ if there is only a single photon in the final state, where f_γ is the photon occupation number. For our halo,

$$f_\gamma = f_{\gamma,\mathrm{CMB}}(\nu) + f_{\gamma,\mathrm{ext-bkg}}(\nu) + f_{\gamma,\mathrm{gal}}(\nu; l, b), \qquad (12)$$

where the three components represent the cosmic microwave background ($T_{\mathrm{CMB}} = 2.725\,K$), the extragalactic radio background ($T_{\mathrm{ext\text{-}bkg}} \approx 0.78\,K$ in the middle of our frequency range), and the Galactic diffuse emission. The CMB and the extragalactic radio background are isotropic, whereas the Galactic diffuse emission is sharply peaked around the Galactic center, which being largely below the GBT horizon can be neglected for this analysis. The enhancement factor f_γ for our analysis ranges from approximately 49 at 1350 MHz to 21 at 2650 MHz.

The current MeerKAT and future Square Kilometer Array will have the benefit of the very large Bose–Einstein enhancement factor associated with the Galactic diffuse emission ($2f_\gamma \approx 10^{(3-4)}$ for the comparable L-band range as studied here), which could result in sensitivity exceeding current Horizontal Branch Star and CAST limits (V. Anastassopoulos et al. 2017).

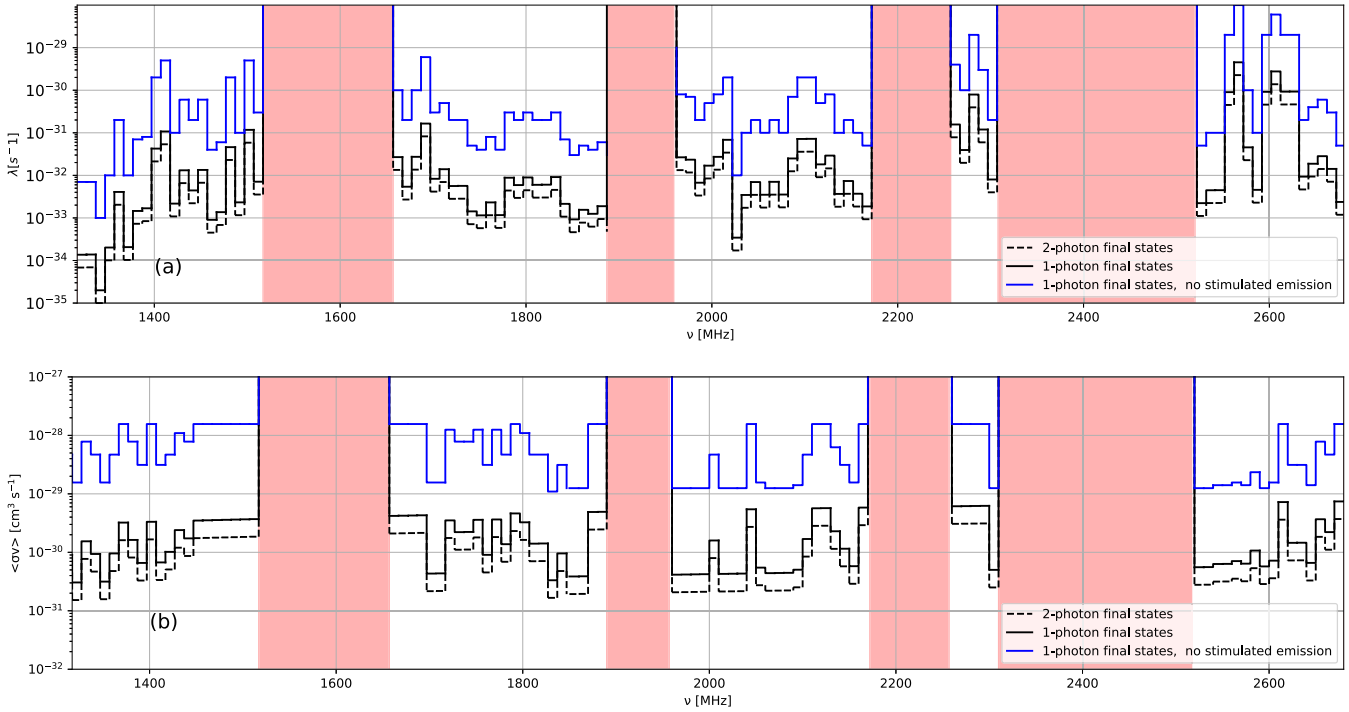

Figure 5. (a) Decay limits in the *L* and *S* bands, with excluded regions highlighted in red (for reasons of high noise or damping). (b) Annihilation limits in the *L* and *S* bands. This figure corrects the absolute value of the velocity-weighted cross section appearing in A. Keller et al. (2022) for the frequency range 1710–1840 MHz. In both cases, 1-photon final states (solid line), 2-photon final states (dashed line), and 1-photon states without the effect of stimulated emission (blue solid line) are shown.

4. Conclusion

In summary, we have now applied our analysis methodology in the *L* and *S* bands to set model-independent limits on dark matter over an octave in frequency. More generally, this analysis demonstrates that signals from nonlocalized sources that are both weak and broad ($\approx m$Jy, $\frac{\Delta\nu}{\nu} \approx 10^{-3}$) can be readily detected at high confidence level. This will be an important tool in searching for the recently predicted axion clouds surrounding neutron stars, an extremely dense ($10^{22}\,\mathrm{GeV\,cm^{-3}}$) gravitationally trapped population of axions whose late-stage width can be as large as 10^{-2} (D. Noordhuis et al. 2024).

More immediately, the analysis is being extended to the *C*- and *X*-band data sets in the BL public data release.

Acknowledgments

We gratefully acknowledge the support of the Heising-Simons Foundation, grants 2018-0989 and 2022-3566, and the assistance of Andrew Siemion, Steve Croft, and Matt Lebofsky of the Breakthrough Listen program throughout the project. The Breakthrough Prize Foundation funds the Breakthrough Initiatives, which manages Breakthrough Listen. The Green Bank Observatory facility is supported by the National Science Foundation and is operated by Associated Universities, Inc. under a cooperative agreement. N.W. was funded as a participant in the Berkeley SETI Research Center Research Experience for Undergraduates Site, supported by the National Science Foundation under Grant No. 2244242. A.K. acknowledges receipt of a graduate research grant from the Applied Science and Technology program.

ORCID iDs

Aya Keller https://orcid.org/0000-0002-9036-3598
Nicole Wolff https://orcid.org/0009-0006-1306-0928
Karl van Bibber https://orcid.org/0000-0002-1702-1292

References

Anastassopoulos, V., Aune, S., Barth, K., et al. 2017, NatPh, 13, 584
Aprile, E., Aalbers, J., Agostini, F., et al. 2019, PhRvL, 122, 141301
Backes, K. M., Palken, D. A., Kenany, S. A., et al. 2021, Natur, 590, 238
Ben, B., Flöer, L., Keller, R., et al. 2016, A&A, 594, A116
Caputo, A., Regis, M., Taoso, M., & Witte, S. J. 2019, JCAP, 1903, 027
Keller, A., O'Brien, S., Kamdar, A., et al. 2022, ApJ, 927, 71
Kuhn, H. W. 1955, Nav. Res. Logist. Q., 2, 83
Lebofsky, M., Croft, S., Siemion, A. P., et al. 2019, PASP, 131, 1006
Monari, G., Famaey, B., Carrillo, I., et al. 2018, A&A, 615, L1
Navarro, J. F., Frenk, C. S., & White, S. D. M. 1997, ApJ, 490, 493
Nesti, F., & Salucci, P. 2013, JCAP, 2013, 016
Noordhuis, D., Prabhu, A., Weniger, C., & Witte, S. J. 2024, PhRvX, 14, 041015
Pillepich, A., Kuhlen, M., Guedes, J., & Madau, P. 2014, ApJ, 784, 161
Price, D. C., Enriquez, J. E., Brzycki, B., et al. 2020, AJ, 159, 86
Speckhard, E. G., Ng, K. C. Y., Beacom, J. F., & Laha, R. 2016, PhRvL, 116, 031301